

Computation of Optical Refractive Index Structure Parameter from its Statistical Definition Using Radiosonde Data

Florian Quatresooz*, Danielle Vanhoenacker-Janvier[‡], Claude Oestges[§]
 ICTEAM - Université catholique de Louvain - Louvain-la-Neuve, Belgium

*florian.quatresooz@uclouvain.be, [‡]danielle.vanhoenacker@uclouvain.be, [§]claudio.oestges@uclouvain.be

Abstract—Knowledge of the optical refractive index structure parameter C_n^2 is of interest for Free Space Optics (FSO) and ground-based optical astronomy, as it depicts the strength of the expected scintillation on the received optical waves. Focus is given here to models using meteorological quantities coming from radiosonde measurements as inputs to estimate the C_n^2 profile in the atmosphere. A model relying on the C_n^2 statistical definition is presented and applied to recent high-density radiosonde profiles at Trappes (France) and Hilo, HI (USA). It is also compared to thermosonde measurements coming from the T-REX campaign. This model enables to obtain site-specific average profiles and to identify isolated turbulent layers using only pressure and temperature measurements, paving the way for optical site selection. It offers similar performance when compared to a Tatarskii-based model inspired by the literature.

Index Terms—Free space optics, optical turbulence, scintillation, radiosonde, atmospheric propagation.

I. INTRODUCTION

Earth-to-satellite optical communications and ground-based optical astronomy share a common interest: the characterization of atmospheric effects on the propagation of optical waves. Optical turbulence is one of these effects and arises from random fluctuations of the refractive index due to atmospheric turbulence. This phenomenon is behind the twinkling of stars and the need for adaptive optics to correct optical observations. It has been studied by astronomers for more than 40 years and numerous models have been designed [1]. However, one should be cautious when applying these models to optical communication sites since atmospheric conditions different than at astronomical sites are expected [2]. Hence, extra work on this topic is needed.

Commonly, electro-optical engineers are interested in the scintillation effects on the received electromagnetic waves, such as the scintillation index σ_I^2 or the variance of the log-amplitude fluctuations σ_χ^2 . Under some hypotheses, they directly depend on the refractive index structure parameter C_n^2 through analytical expressions [3]–[5]. C_n^2 is a parameter that describes the intensity of atmospheric refractive index fluctuations and its knowledge enables to perform flexible scheduling or ground site selection (e.g. by avoiding hours or areas with large turbulence). It is also of particular interest for adaptive optics and for the design of optical communication systems. C_n^2 varies with time (hours of the day and seasons), as well as with space: it depends on the location on Earth and on the altitude. The altitude dependence of C_n^2 leads to C_n^2 profiles, which are interesting for ground-to-satellite communications crossing the whole atmosphere.

Measurements of C_n^2 profiles are not always practical since they require the use of dedicated tools (e.g. thermosondes).

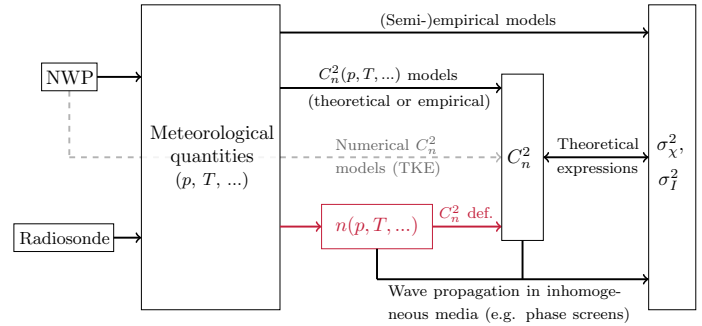


Fig. 1: Main scintillation quantities and associated links.

Moreover, some tools can only provide integrated quantities of C_n^2 profiles, such as the seeing that can be obtained with a differential image motion monitor for example [6]. Hence, throughout the years, several models have been designed to determine C_n^2 profiles based only on atmospheric quantities, namely using meteorological quantities.

Different approaches classically found in the literature are depicted in Fig. 1. Meteorological quantities can come from radiosonde measurements or from numerical weather prediction (NWP) simulations; the latter enabling the prediction of future C_n^2 profiles based on current weather forecast. From these quantities, empirical (e.g. Dewan model [7], Hufnagel-Valley model [5], [8]) or theoretical (e.g. Tatarskii [3]) models can be used to determine C_n^2 . Alternatively, NWP software can directly solve for C_n^2 using the turbulent kinetic energy (TKE), see [9], [10]. There also exist other approaches to characterize the scintillation index σ_I^2 or the variance σ_χ^2 without relying on C_n^2 , such as statistical models with probabilistic distributions (e.g. [5], [11]). Approaches involving wave propagation in inhomogeneous media are also possible, for example making use of phase screens (e.g. [12]), but are not considered here.

Regarding the determination of C_n^2 profiles based on meteorological quantities, focus will be given here to radiosonde measurements as they have an improved spatial resolution compared to NWP simulation data, especially in the vertical direction [13].

For microwave scintillation, [14] presents a probabilistic model of C_n^2 deduced from radiosondes that does not rely on empirical relationships derived from particular experiments. In [15], a C_n^2 approach relying on its statistical definition is introduced to compute complementary cumulative distribution functions (CCDF) of microwave scintillation. This statistical definition approach is further extended in this work and applied to optical scintillation.

In optics, one can use radiosonde measurements to pa-

parameterize C_n^2 models, such as the Dewan model [7] or the Trinet-Vernin model [16]. Equivalently, analytical expressions of C_n^2 can be used with meteorological quantities coming from radiosonde measurements. Usually, such expressions involve the computation of vertical gradients based on the Tatarskii model of C_n^2 [3]. Even though this approach has a theoretical basis, models of the refractive index gradient M and the outer scale of turbulence L_0 must still be chosen, as for example in [17], [18]. This is also the approach followed in [19], [20], where C_n^2 profiles computed with meteorological data from radiosonde measurements are then compared to C_n^2 measurements coming from thermosondes. A similar model is used in [21] but using meteorological quantities coming from NWP simulations instead of radiosonde measurements. Alternative expressions using the Thorpes or the Ellison scales instead of the outer scale L_0 are also possible, as applied in [22], [23], and [24].

In this paper, C_n^2 is derived from its statistical definition involving the optical refractive index. This latter is computed based on meteorological quantities coming from radiosondes. This is the approach highlighted in red in Fig. 1, that is motivated by its simplicity. Nevertheless, it provides time- and location-dependent C_n^2 profiles based on meteorological quantities at a given time and at a specified location. Hence, the following contributions are added in this paper:

- 1) An optical C_n^2 model relying on its statistical definition is presented, with all steps explained to extract the refractive index fluctuations based on vertical profiles of temperature and pressure only.
- 2) The presented model can be applied to any place in the world where high-density radiosonde profiles are available. It is therefore not limited to astronomical observation sites and is of particular interest for optical communication ground terminals.
- 3) A fitting of parametric profiles is also conducted, enabling to obtain site-specific average C_n^2 models that can be useful for optical site selection.

First, Section II presents the C_n^2 models used in this paper. They are then validated in Section III using radiosonde observations at Trappes (France) and Hilo, HI (USA), as well as thermosonde measurements from the T-REX campaign. Finally, Section IV summarizes the physical limitations of the presented model.

II. DESCRIPTION OF C_n^2 MODEL

The C_n^2 models presented here mainly depend on the theory that describes the refractive index as a random field. The latter is firstly reminded up to the introduction of C_n^2 . The Tatarskii C_n^2 model is then presented and our alternative approach relying on the C_n^2 statistical definition is detailed.

A. The refractive index as a random field

In the framework of turbulence, the refractive index n is a stochastic function of time (t) and space ($\mathbf{r} = (r_x, r_y, r_z)$), i.e. a space-time random field, denoted $n(\mathbf{r}, t)$. Commonly, it is written [5]:

$$n(\mathbf{r}, t) = n_0(\mathbf{r}, t) + n_1(\mathbf{r}, t), \quad (1)$$

where $n_0(\mathbf{r}, t) = \langle n(\mathbf{r}, t) \rangle$ is the mean value of $n(\mathbf{r}, t)$, and $n_1(\mathbf{r}, t)$ corresponds to the fluctuation of the refractive index around its mean. By definition, $\langle n_1(\mathbf{r}, t) \rangle = 0$. All means are expressed as ensemble averages, e.g.

$$n_0(\mathbf{r}, t) = \langle n(\mathbf{r}, t) \rangle = \int_{-\infty}^{+\infty} n T_n(n, \mathbf{r}, t) dn, \quad (2)$$

with $T_n(n, \mathbf{r}, t)$ the probability density function of the refractive index.

The optical refractive index can be expressed as a function of atmospheric quantities, namely the pressure and the temperature [5]:

$$n = 1 + 77.6 \times 10^{-6} \left(1 + 7.52 \times 10^{-3} \lambda^{-2} \right) \frac{p}{T}. \quad (3)$$

In (3), p is the pressure in hectopascal [hPa] and T is the temperature in kelvin [K]. They can both be function of the position \mathbf{r} and the time t . The wavelength λ is in micrometer [μm] and is often considered to be $0.5 \mu\text{m}$, leading to the following approximate expression:

$$n \approx 1 + 79 \times 10^{-6} \frac{p}{T}. \quad (4)$$

Therefore, fluctuations of pressure and temperature lead to fluctuations of the optical refractive index. Disregarding time variations of the refractive index, the structure function of the refractive index fluctuations between two positions in space (\mathbf{r}_1 and \mathbf{r}_2) is [3]

$$D_n(\mathbf{r}_1, \mathbf{r}_2) = \left\langle (n_1(\mathbf{r}_1) - n_1(\mathbf{r}_2))^2 \right\rangle. \quad (5)$$

Assuming local homogeneity, the structure function depends only on the position difference, i.e. $\boldsymbol{\rho} = \mathbf{r}_1 - \mathbf{r}_2$. Adding the isotropy hypothesis, only the absolute distance difference $\rho = |\boldsymbol{\rho}|$ matters and not its orientation. With these two assumptions, the structure function is now expressed as in [4]:

$$D_n(\rho) = \left\langle (n_1(\mathbf{r} + \boldsymbol{\rho}) - n_1(\mathbf{r}))^2 \right\rangle. \quad (6)$$

Based on the Kolmogorov cascade theory of turbulence, the structure function is shown to be proportional to $\rho^{2/3}$, the proportionality factor being the refractive index structure constant C_n^2 [$\text{m}^{-2/3}$]. This is only valid between the inner scale l_0 and the outer scale L_0 , that depict the range where turbulent eddy energy is transferred from larger eddies to smaller eddies (inertial range) [3]–[5]. Thus the structure function can be written as

$$D_n(\rho) = C_n^2 \rho^{2/3} \quad \text{for} \quad l_0 < \rho < L_0. \quad (7)$$

Equation (7) is associated to the Kolmogorov power spectrum $\Phi_n(\kappa) = 0.033 C_n^2 \kappa^{-11/3}$ for $1/L_0 \ll \kappa \ll 1/l_0$, where κ is the spatial frequency. The link between these quantities is given by the following integral [5]:

$$D_n(\rho) = 8\pi \int_0^{+\infty} \kappa^2 \Phi_n(\kappa) \left(1 - \frac{\sin(\kappa\rho)}{\kappa\rho} \right) d\kappa. \quad (8)$$

In practice, the turbulence characteristics vary with the altitude z and so does C_n^2 . This leads to a C_n^2 profile denoted $C_n^2(z)$.

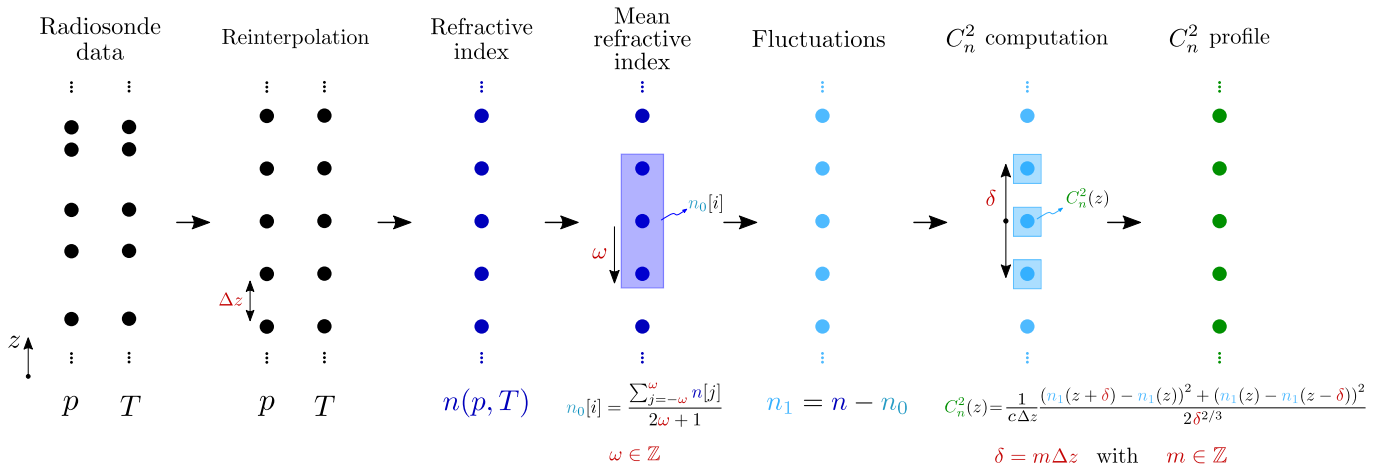


Fig. 2: Followed approach to extract C_n^2 from its statistical definition. The three parameters (δ , ω and ρ) that can be chosen are depicted in red; c is a calibration parameter.

B. Tatarskii-based C_n^2 model

Built on Kolmogorov theory, an expression of C_n^2 as a function of the outer scale L_0 and the refractive index vertical gradient $M = \frac{\partial n}{\partial z}$ has been presented by [3]:

$$C_n^2 = a^2 L_0^{4/3} M^2, \quad (9)$$

where a^2 is usually set to 2.8 [25]. Equation (9) is quite generic and requires expressions for L_0 and M . In the following, M is chosen as in [26],

$$M = -\frac{80 \times 10^{-6} p}{T\theta} \frac{\partial \theta}{\partial z}, \quad (10)$$

with θ the potential temperature. For L_0 , an extension of the [7] model, named HMNSP99, is used, as presented in [24], [27], [28]:

$$L_0^{4/3} = 0.1^{4/3} \times 10^Y, \quad (11)$$

with

$$Y = \begin{cases} 0.362 + 16.728 S - 192.347 \frac{\partial T}{\partial z} & \text{in the troposphere,} \\ 0.757 + 13.819 S - 57.784 \frac{\partial T}{\partial z} & \text{in the stratosphere.} \end{cases} \quad (12)$$

This is an empirical model derived from measurements in New Mexico, where S is the vertical shear of the horizontal wind velocity. In the rest of this paper, the C_n^2 model from (9) with (10) and (11) will be referred to as the Tatarskii model, and serve as a literature-based model useful to validate the new approach presented in the next section.

C. C_n^2 from statistical definition

An alternative approach to obtain C_n^2 can make use of its statistical definition. Indeed, in the inertial range, (6) and (7) can be used to extract C_n^2 from

$$C_n^2 = \frac{\langle (n_1(\mathbf{r} + \boldsymbol{\rho}) - n_1(\mathbf{r}))^2 \rangle}{\rho^{2/3}} \quad \text{for } l_0 < \rho < L_0. \quad (13)$$

Computation of (13) is not straightforward and implies several steps detailed below and depicted in Fig. 2.

First, one assumes to have access to vertical profiles of the pressure p and the temperature T . Such profiles are provided by radiosondes for example, as shown on the left part of Fig. 2. The vertical z -direction is altitude whereas black points depict positions where measurements of pressure and temperature are available. In the case of radiosondes, vertical sampling is unlikely to be equispaced. Data are then resampled to a constant vertical spacing denoted Δz using linear interpolation. Indeed, the last step of our C_n^2 computation requires a fixed vertical spacing between the points, see (14) detailed below.

Next, the refractive index is computed using (3) or (4) depending on the knowledge of the wavelength and the choice of taking it into account (the variations of the optical C_n^2 with the wavelength can therefore be modeled with this approach). This provides a vertical profile of the refractive index (third step in Fig. 2).

In (13), only the fluctuations n_1 of the refractive index are involved but not directly the refractive index n itself. Thus, there is a need to extract the refractive index mean n_0 , and then obtain the fluctuations with $n_1 = n - n_0$. The mean should be computed locally based on neighboring points. For this reason, a window mean of size $2\omega+1$ is used, with $\omega \in \mathbb{Z}$ (steps 4 and 5 in Fig. 2).

Eventually, the C_n^2 profile is computed using

$$C_n^2(z) = \frac{1}{c \Delta z} \frac{(n_1(z+\delta) - n_1(z))^2 + (n_1(z) - n_1(z-\delta))^2}{2 \delta^{2/3}}. \quad (14)$$

The ensemble average in (13) is substituted by a three-point average between points spaced by a vertical spacing δ . This vertical spacing is a multiple of the vertical resolution Δz (see Fig. 2). Due to the vertical sampling, a factor Δz arises at the denominator to ensure the homogeneity of (14). This is justified in A. Finally, c is a calibration parameter named *scale factor*. Its origin is motivated in Section II-D and, as it is shown in the next sections, this parameter does not seem to depend on the location.

With the presented approach, three parameters must be chosen:

- 1) the vertical spacing Δz used for resampling the data;

- 2) the integer ω depicting the window size used for the computation of the mean refractive index;
- 3) the vertical spacing $\delta = m \Delta z$ with $m \in \mathbb{Z}$ used for computing the average in the C_n^2 expression.

At this stage, some limitations of the approach can already be identified:

- 1) The computation of the local refractive index mean n_0 to extract the fluctuations is difficult. Indeed, the window for computing the mean must not be too large as the refractive index mean value varies with altitude due to variations of the mean pressure and temperature with altitude.
- 2) The available vertical resolution of the input meteorological data can also limit the approach and the choice of Δz . If the resolution is too low, it is unlikely that the computed mean will be representative of the local refractive index mean n_0 . Furthermore, the choice of Δz must be related to the vertical extent of the turbulent structures to be identified. For example, large Δz (e.g 400 m) are useful to obtain average profiles smoothed out of noisy artefacts but do not enable to detect thin turbulent layers.
- 3) The first point of the profile is ideally located at an altitude $\delta + \omega \Delta z$ in order to compute the mean refractive index and C_n^2 following Fig. 2. Otherwise, neighboring points are missing to perform the computations. This means that the presented model is unable to depict close to ground turbulence, especially if Δz is large.
- 4) The presented approach is only valid between the inner scale l_0 and outer scale L_0 . The inner scale is unlikely to be an issue as it is on the order of millimeter or centimeter [5]. On the contrary, the outer scale spans from meters to hundreds of meters [29], [30] and can limit our computation (see Section II-D and Section IV).

D. Synthetic data

In order to validate the statistical definition approach and determine the impacts of some parameters, such as ω or the outer length L_0 , a preliminary analysis is performed with synthetic data. A study of the limitations related to the outer scale L_0 is of particular interest since, in practical scenarios, this scale is often found to be smaller than 10 meters [17], [25], [29]. However, in Section III, radiosonde observations with a vertical resolution on the order of 10 meters will be used, with a resampling distance Δz between 25 and 400 meters. Hence, the assumption about the inertial range, required for applying (13), may not hold, and this impact is studied here.

For this study with synthetic data, one-dimensional (1D) fluctuations of the refractive index have been generated through white noise coloring to obtain the desired properties (i.e. the desired spatial power spectrum) on the resulting fluctuations. In order to include the limitations imposed by the outer scale L_0 in the simulation, the von Kármán spectrum has been chosen [5]:

$$\Phi_n(\kappa) = \frac{0.033 C_n^2}{(\kappa^2 + \kappa_0^2)^{11/6}}, \quad (15)$$

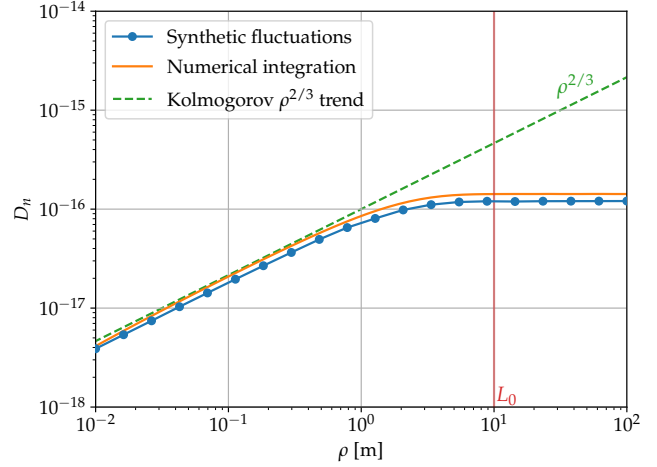


Fig. 3: Structure function from 1D simulations.

with $\kappa_0 = 1/L_0$. The associated 1D power spectrum $V_n(\kappa)$ is found thanks to [5]:

$$\Phi_n(\kappa) = -\frac{1}{2\pi\kappa} \frac{dV_n(\kappa)}{d\kappa}. \quad (16)$$

Figure 3 represents the structure function computed from the simulated fluctuations using (6), substituting the ensemble average by a spatial average. The chosen parameters for the simulation are: $L_0 = 10$ m and $C_n^2 = 10^{-16} \text{ m}^{-2/3}$. The structure function is computed for several spacing ρ and compared to the Kolmogorov trend, from (7). Agreement is indeed reached in the inertial range (i.e. between l_0 , assumed to be 0 here, and L_0), even though the structure function tends to be slightly underestimated. Numerical integration of (8) with the von Kármán spectrum is also depicted, highlighting the saturation of the structure function above the outer scale L_0 .

Figure 4 shows the scale factor c for $C_n^2 = 10^{-16} \text{ m}^{-2/3}$ and an outer scale L_0 varying from 1 to 100 meters. This factor is defined as the ratio between the estimated C_n^2 (i.e. the one recovered using the statistical definition method on the simulated data) and the real C_n^2 (i.e. the one applied as an input in the generation of synthetic data). C_n^2 is estimated assuming different spatial resolutions Δz , with $\delta = \Delta z$ and varying window size ω for the mean estimation.

For resolution sufficiently smaller than the outer scale (roughly one order of magnitude), the estimated C_n^2 and the simulation value are close since the factor is a bit lower than one. In other words, there is a small underestimation of C_n^2 , mostly coming from an underestimation of the fluctuations n_1 when extracting the mean. Indeed, neighboring fluctuations are correlated, meaning that the extracted mean does not only contain n_0 but also a non-zero mean of neighbored fluctuations n_1 . Therefore, fluctuations tend to be underestimated and so is C_n^2 . Increasing the window size ω enables to look at more points that are also further from each other, with less correlated fluctuations, improving the extracted mean n_0 and therefore reducing the underestimation of fluctuations.

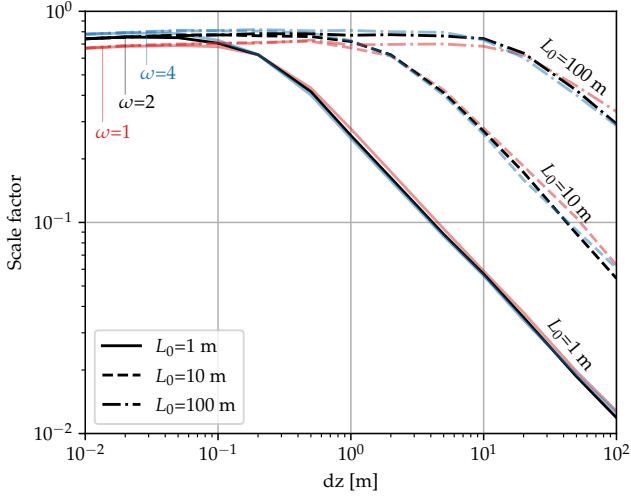


Fig. 4: Scale factor for C_n^2 correction on synthetic data. Colors depict the choice of the window size parameter ω .

For spacing Δz close to or larger than L_0 , the factor starts to decrease following a minus two-third power trend. Indeed, the validity of (13) is not ensured anymore: as observed in Fig. 3, the structure function tends to saturate. Since this structure function is exactly the numerator in (13), only the influence of its denominator remains, that corresponds exactly to a minus two-third power trend. If observed with real-world measurements, such a decrease of the scale factor c would be a hint that the outer scale L_0 has been reached. A possible approach to obtain the factor c for C_n^2 profiles based on radiosonde measurements is presented in Section III-A.

III. VALIDATION OF THE C_n^2 MODELS THROUGH DATA ANALYSIS

In this section, both C_n^2 models presented in Section II, i.e. the Tatarskii model and the statistical definition model, are applied to radiosonde measurements for validation. As a first step, the statistical definition model is calibrated thanks to the Hufnagel-Valley model.

A. Calibration using Hufnagel-Valley model

Calibration of the statistical definition model refers to the determination of the scale factor c in practical scenarios. This can be achieved by comparing obtained C_n^2 profiles with empirical models from the literature, such as the Hufnagel-Valley model. A generalisation of this model is presented in [31]:

$$C_n^2(z) = A \exp\left(-\frac{z}{H_A}\right) + B \exp\left(-\frac{z}{H_B}\right) + C \left(\frac{z}{10^5}\right)^{10} \exp\left(-\frac{z}{H_C}\right) + D \exp\left(-\frac{(z-H_D)^2}{2d^2}\right), \quad (17)$$

with z the altitude above sea level [m]. Equation (17) involves several coefficients: A , B , C , and D , that have the units of a

C_n^2 [$\text{m}^{-2/3}$], and H_A , H_B , H_C , and H_D , that are expressed in [m]. The first term in (17) depicts the surface turbulence, the second term represents the troposphere turbulence whereas the third term defines the turbulence at the tropopause. Moreover, there is a fourth term representing isolated layers of turbulence with a Gaussian shape of thickness d . This term is repeated if there are several turbulent layers.

Usually, the Hufnagel-Valley 5/7 profile (HV-5/7) is used in astronomy and for optical communications [5]. Its expression is a particular case of (17):

$$C_n^2(z) = A \exp\left(-\frac{z}{100}\right) + 2.7 \times 10^{-16} \exp\left(-\frac{z}{1500}\right) + 0.00594 \left(\frac{w}{27}\right)^2 \left(\frac{z}{10^5}\right)^{10} \exp\left(-\frac{z}{1000}\right), \quad (18)$$

where A is the C_n^2 value near the ground [$\text{m}^{-2/3}$], and w is the root-mean-square high altitude wind speed [m/s]. The HV-5/7 profile is obtained with $w = 21$ m/s and $A = 1.7 \times 10^{-14} \text{m}^{-2/3}$.

The important observation in (18) is the B coefficient that is set to a constant value of 2.7×10^{-16} . It leads to a fixed range in the Hufnagel-Valley model (between 1 and 4 km of altitude), that is independent of the other parameters w and A , as depicted in Fig. 5. This remarkable feature is most probably related to the relatively constant temperature and pressure mean lapse rate in the troposphere.

When applying the statistical definition C_n^2 model to radiosonde data, the same constant slope (on a semilogarithmic representation) has been observed in the 1 to 4 km region. Hence, this characteristic can be exploited to calibrate the obtained C_n^2 profiles in order to ensure a good fit between these profiles and the HV-5/7 profile in this region. This is illustrated at Trappes (France) and Hilo, HI (USA), in Sections III-B and III-C.

B. Application to radiosonde measurements at Trappes, France

High-density profiles from the University of Wyoming (UWYO) Atmospheric Science Radiosonde Archive¹ have been used as input meteorological data. Data collected above Trappes (latitude 48.77° N, longitude 2.01° E, altitude 168 meters) in France during the year 2020 have been analyzed. Radiosondes are launched twice a day, at 00h00 and 12h00 UTC. They offer a vertical resolution of 10 meters (standard deviation: 3 m) nearly independent of the altitude, and provide altitude, pressure, temperature, relative humidity, wind speed and wind direction profiles. Moreover, radiosonde drifting due to wind has been neglected, meaning that C_n^2 profiles obtained are considered at zenith while in fact they are obtained along the radiosonde trajectory. This drifting is spatially limited since, for example, for the year 2020 at Trappes, the average drift (computed at the altitude of 20 km following [32] with a mean ascent rate of 6 m/s) is close to 50 km, with a standard deviation of 28 km. It is also not expected to influence the vertical resolution as the radiosonde directly records the

¹<http://weather.uwyo.edu/upperair/buffraob.shtml>

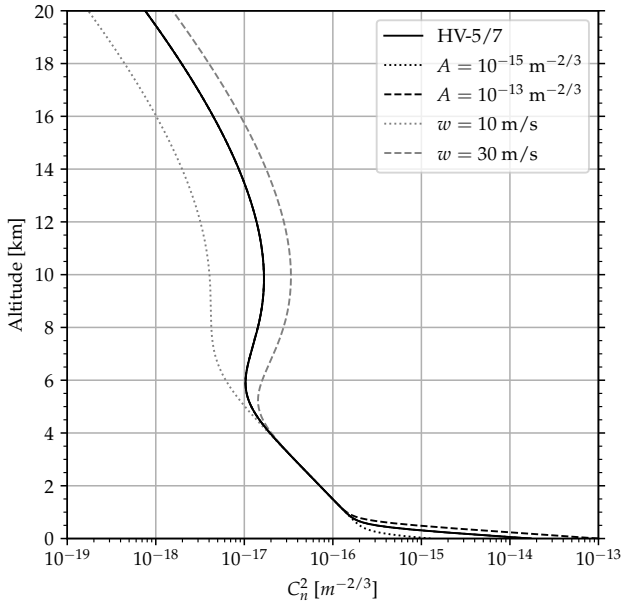


Fig. 5: Hufnagel-Valley model variations with w and A parameters. If not specified, parameters used are the ones of HV-5/7.

altitude above ground and not the distance traveled by the balloon.

Following the approach presented in Section II-C, C_n^2 profiles have been computed for each available measurement, neglecting the days where the radiosonde did not reach the altitude of 30 km. In total, 630 different C_n^2 profiles have been obtained and computed with different vertical spacings Δz . The averages of these profiles are presented in Fig. 6 for Δz of 50, 100 and 200 meters. For all C_n^2 computations, parameter ω has been set to 2 whereas δ was equal to the Δz -spacing. The approximate model of n from (4) has been used. The altitude corresponds to the altitude above ground (and not above the mean sea level). For comparison, the Tatarskii C_n^2 model has also been added, directly computed from the radiosonde measurements and using a troposphere maximum altitude of 10 km in (11).

All three profiles of Fig. 6 coming from the C_n^2 statistical definition have been calibrated with their associated scale factor. Computation of these calibration ratios has been performed using the methodology explained in Section III-A, i.e. by ensuring agreement with the HV-5/7 profile in the 1-4 km region. Such agreement is indeed achieved, as can be seen on the zoom in Fig. 6, using the factors given in Table I, with $\omega = 2$ and $\delta = \Delta z$. They have been obtained by first computing the ratio between the modeled C_n^2 value and the HV-5/7 C_n^2 value for each point in the 1-4 km region, then taking the average. The standard deviation is also given.

These scale factors are independent of the altitude and the initial radiosonde vertical resolution. They vary slightly with the window size parameter ω and the vertical spacing δ . Surprisingly, the values obtained do not show the $\Delta z^{-2/3}$

TABLE I: Scale factors depending on Δz - mean value and standard deviation.

Δz [m]	Scale factors c		
	$\omega = 1, \delta = \Delta z$	$\omega = 2, \delta = \Delta z$	$\omega = 2, \delta = 2\Delta z$
25	0.47 ± 0.12	0.60 ± 0.12	0.60 ± 0.1
50	0.37 ± 0.06	0.53 ± 0.08	0.57 ± 0.08
100	0.36 ± 0.04	0.53 ± 0.05	0.58 ± 0.06
200	0.36 ± 0.03	0.51 ± 0.04	0.56 ± 0.05
400	0.35 ± 0.01	0.48 ± 0.01	0.51 ± 0.02

trend that is observed in the simulation values in Fig. 4 for Δz larger than the outer scale L_0 . This may hint that the outer scale has not been reached yet, and that constraints on ρ in (7) can be relaxed, or, at least, are partially hidden by the calibration with the scale factor c . In the following, the scale factor $c = 0.5$ is chosen for $\omega = 2$ and $\delta = \Delta z$, for all Δz .

With the calibration, C_n^2 profiles coming from the statistical definition in Fig. 6 tend to superimpose. They all contain a large ground C_n^2 value and a fixed slope from 1 to 6 kilometers of altitude, that exactly corresponds to the same slope as in the HV-5/7 model. The slope in this region for the Tatarskii model is slightly different. There is then a bump in the C_n^2 profile, around 12 km of altitude, that is related to the altitude of the tropopause and the associated constant temperature and large wind shears. This bump is also observed in the Tatarskii model. After the tropopause, C_n^2 slowly decreases again and starts experiencing some fluctuations related to the reinterpolation process. This mostly comes from the small variations of the atmospheric quantities at these altitudes that cannot be recorded by the radiosondes as well as from the uneven and larger vertical sampling distance of radiosondes at high altitudes.

Interestingly, the shape of C_n^2 profiles is not similar to the HV-5/7 model above the altitude of 6 kilometers. This is because the free atmosphere part of the Hufnagel-Valley model has been derived based on radiosonde measurements over New Mexico [8] and is therefore sensitive to the location where the measurements have been made.

Fitting the model in (17) leads to the dashed line in Fig. 6, denoted as *HV fitted*, with the coefficients presented in Table II. The fitting has been performed by minimizing the least square error with the statistical definition C_n^2 profile obtained from radiosonde measurements with $\Delta z=200$ m. The four parameters in blue in Table II have been set prior to the least square fitting. As seen in Fig. 6, good parameterization of the generalized HV profile enables to analytically model the mean C_n^2 profile at a particular location (Trappes, in this case). This offers very simple expressions of average C_n^2 profiles that can be obtained at different locations and compared, e.g. to perform site selection for building optical communication stations.

C. Application to radiosonde measurements at Hilo, HI (USA)

Generalization of the statistical definition C_n^2 model presented in Section II-C and applied to Trappes in Section III-B is further studied by using radiosonde measurements at other locations. In this section, the radio sounding station of Hilo (latitude 19.717° N, longitude 155.05°W, altitude 10

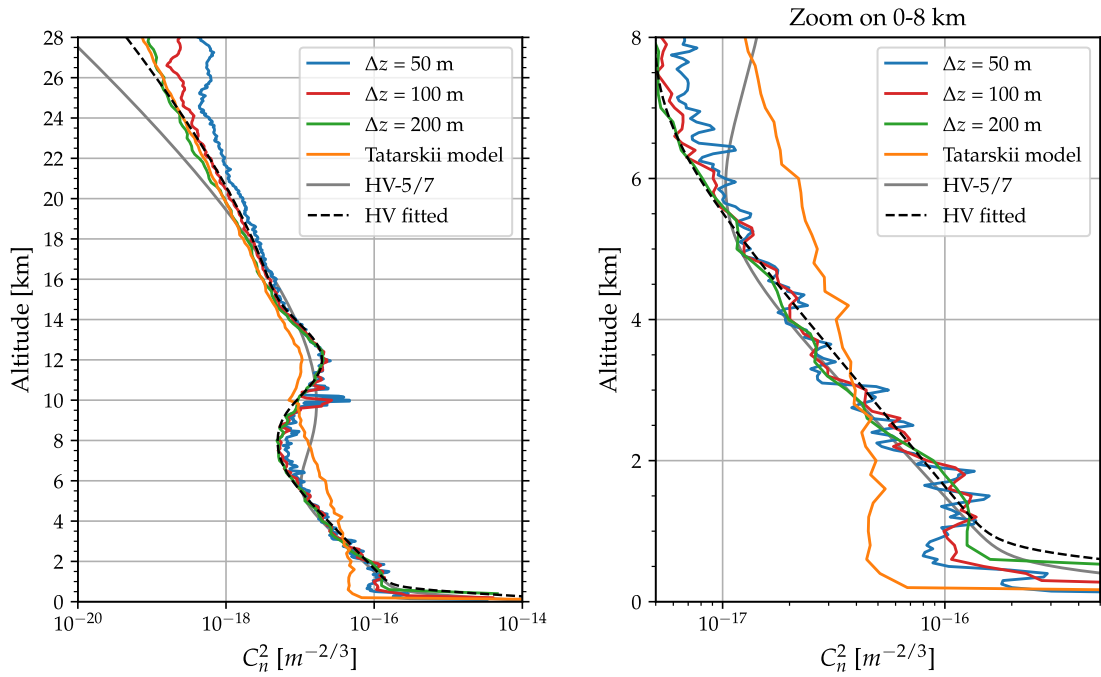


Fig. 6: Average C_n^2 profiles at Trappes for the year 2020, after calibration.

TABLE II: Parameters for generalized HV model in (17).

Parameters	Values for Trappes	Values for Hilo
A [$m^{-2/3}$]	1.32×10^{-13}	4.66×10^{-14}
B [$m^{-2/3}$]	2.7×10^{-16}	2.7×10^{-16}
C [$m^{-2/3}$]	2.07×10^{-4}	2.96×10^{-5}
D [$m^{-2/3}$]	1.37×10^{-17}	4.67×10^{-18}
H_A [m]	100	100
H_B [m]	1645	2006
H_C [m]	1200	1340
H_D [m]	12000	17000
d [m]	1200	1700
E [$m^{-2/3}$]	/	1.59×10^{-16}
H_E [m]	/	2200
e [m]	/	300

meters) at Hawaii (USA), has been chosen, namely because of its completely different location with respect to Trappes and because of the availability of high-density profiles on the University of Wyoming website. A total of 677 radiosonde profiles for the year 2020 have been exploited, offering a vertical resolution of 5 meters (standard deviation: 1 m).

The mean C_n^2 profiles computed with the same ω , δ and scale factors as for Trappes (see Table I) are presented in Fig. 7. Good agreement is achieved between the profiles at different Δz after applying the Trappes scale factors, hinting at the location independence of the factors. Indeed, disregarding the isolated turbulent layer at 2-km of altitude, which origin is discussed below, the slope of the statistical definition C_n^2 profiles is the same as the slope of the Hufnagel-Valley profile ($B = 2.7 \times 10^{-16}$), and quantitative agreement with HV-5/7 is nearly reached using Trappes scaling factors. Furthermore, in Fig. 7, the generalized HV model in (17) has also been fitted, adding another term to model an isolated turbulent layer. All fitted parameters are given in Table II. Compared to the mean profiles at Trappes from Fig. 6, there are two striking

differences:

- 1) The tropopause and its associated turbulent layer is located at a higher altitude, close to 17 km, as given by the parameter H_D . The difference with the classical HV-5/7 model is substantial.
- 2) In addition to the tropopause Gaussian turbulent layer, there is a second isolated layer close to the ground (2 km altitude), modeled by the parameters E (magnitude), H_E (altitude of middle point) and e (thickness). Even though the generalized HV model can depict this turbulent layer, it is unable to represent the reduced turbulence strength below the layer. This layer is also identified in the Tatarskii model, that has been applied using a troposphere's limit of 16 km in (11).

The origins of this second turbulent layer can be seen in Fig. 8. C_n^2 profiles computed with the statistical definition and a Δz of 200 m are presented at Hilo for two different days. On the left graph, a turbulent layer at an altitude of 2 km is noticeable, with C_n^2 reaching nearly $10^{-15} m^{-2/3}$. This layer is associated with a tropospheric temperature inversion arising at this altitude. Indeed, the temperature, depicted in red, starts to increase before decreasing again. Sharp variations of temperature will influence C_n^2 obtained from its statistical definition since the temperature is involved in the computation of the refractive index. On the contrary, on the right graph of Fig. 8, there is no temperature inversion and no turbulent layer is identified. Links between regions of high C_n^2 and temperature inversions have also been identified in [33]. Since temperature inversions close to ground are quite common at Hilo, this explains why this turbulent layer remains noticeable in the mean profile.

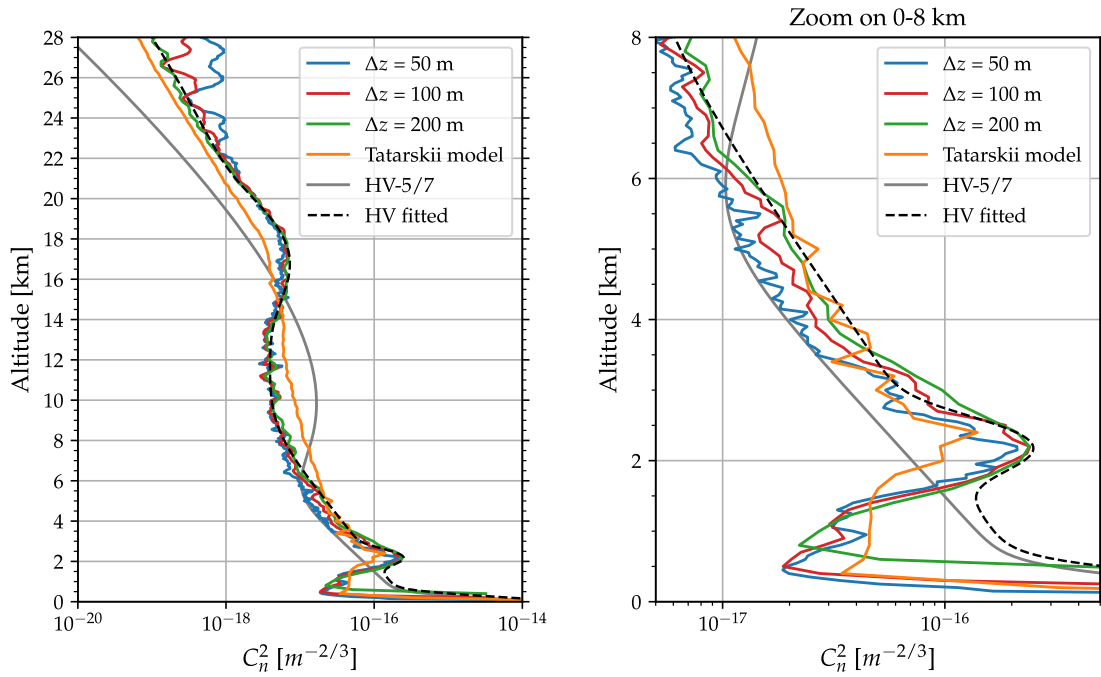


Fig. 7: Average C_n^2 profiles at Hawaii for the year 2020, after calibration.

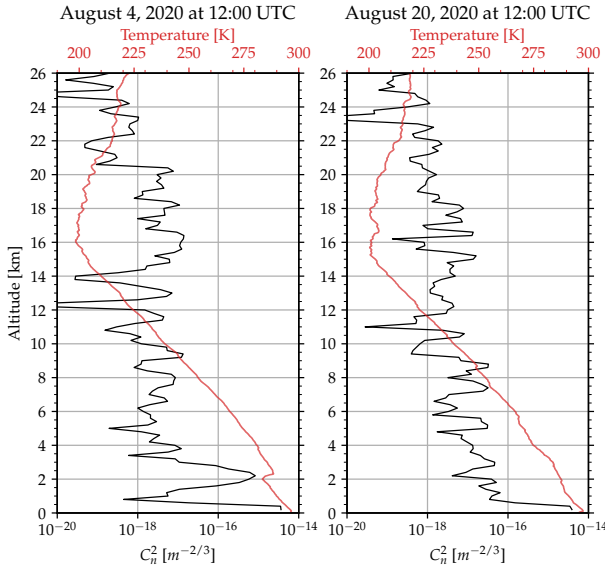


Fig. 8: Two examples of day C_n^2 profiles at Hilo, Hawaii. The C_n^2 model used is the statistical definition model with $\Delta z = 200$ m.

D. Application to T-REX thermosonde measurements at Three Rivers, CA (USA)

Access to thermosonde measurements from the T-REX campaign of the Air Force Research Laboratory (AFRL) has been granted [34]. These data are of particular interest since they include radiosonde measurements as well as thermosonde measurements providing the C_n^2 profile. A comparison between the C_n^2 models (based on radiosonde measurements) and the C_n^2 profile retrieved from the thermosondes is therefore possible.

The T-REX campaign took place from March 20, 2006 to April 6, 2006 in Sierra Nevada Mountains near Three Rivers, CA (launch site: latitude 36.4872° N, longitude 118.84048° W, altitude 503 meters) [35]. The purpose of the experiments was to study higher altitude mountain waves and the associated turbulence. Radiosondes offer a vertical resolution of 10 meters (standard deviation: 3.7 m) recording the altitude, pressure, temperature, relative humidity, wind speed and wind direction.

Thermosondes are able to compute the temperature structure function $D_T(\rho)$ directly based on its definition (similar to (6) but for the temperature) thanks to measurements coming from two temperature sensors spaced by a given distance ρ ($\rho = 1$ m for the T-REX thermosondes) and using a temporal average. Then, the temperature structure parameter C_T^2 is extracted, similarly to (7). Using the pressure and temperature from the radiosonde observations, the temperature structure parameter is finally converted to the refractive index structure parameter C_n^2 thanks to [36]:

$$C_n^2 = \left(\frac{\partial n}{\partial T} \right)^2 C_T^2 = \left(79 \times 10^{-6} \frac{p}{T^2} \right)^2 C_T^2, \quad (19)$$

with p in hectopascal, T in kelvin and the refractive index expression coming from (4).

In total, measurements of 15 different flights have been exploited. Two flights (T-REX011 and T-REX039) have been discarded as they showed strong turbulence up to two orders of magnitude larger than other flights. The remaining 13 flights have been used to compute average C_n^2 profiles. Both C_n^2 models have been applied to the radiosonde measurements, with the statistical definition model using the same parameters as for Trappes (and Hilo), and a Δz of 200 meters. The troposphere's limit is set to 10 km in the Tatarskii model. Regarding the thermosonde measurements, they have been binned and averaged over the same distance Δz . The average

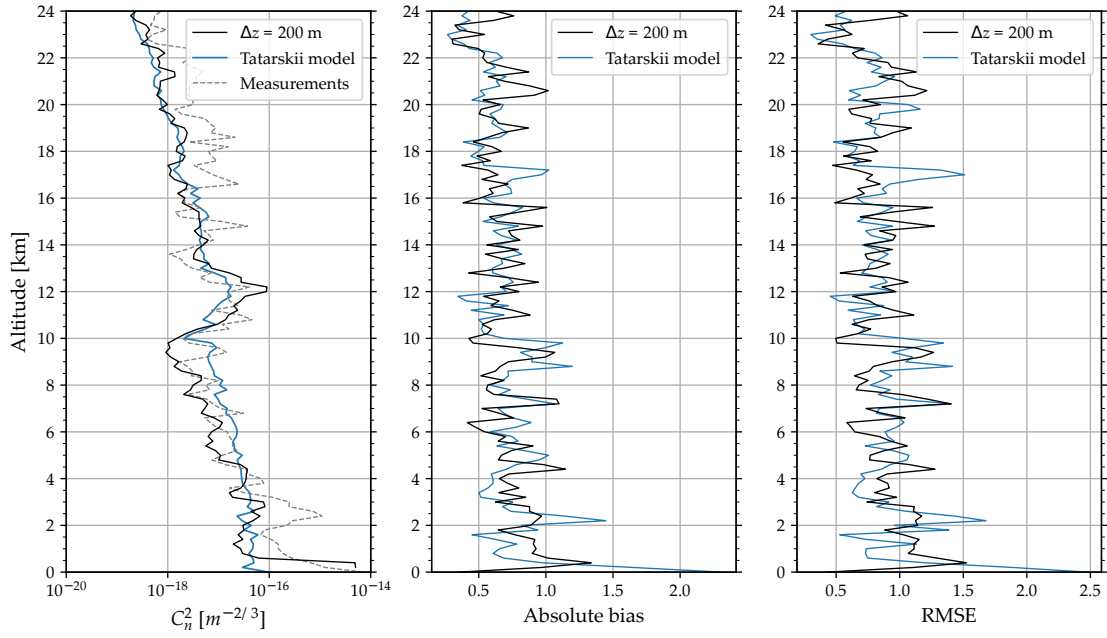


Fig. 9: Average (March 20 - April 26, 2006) profiles for T-REX campaign. *Left:* C_n^2 profiles. *Center:* absolute bias. *Right:* root-mean-square error. Solid lines are the modeled C_n^2 based on radiosonde measurements while the dashed line corresponds to thermosonde measurements.

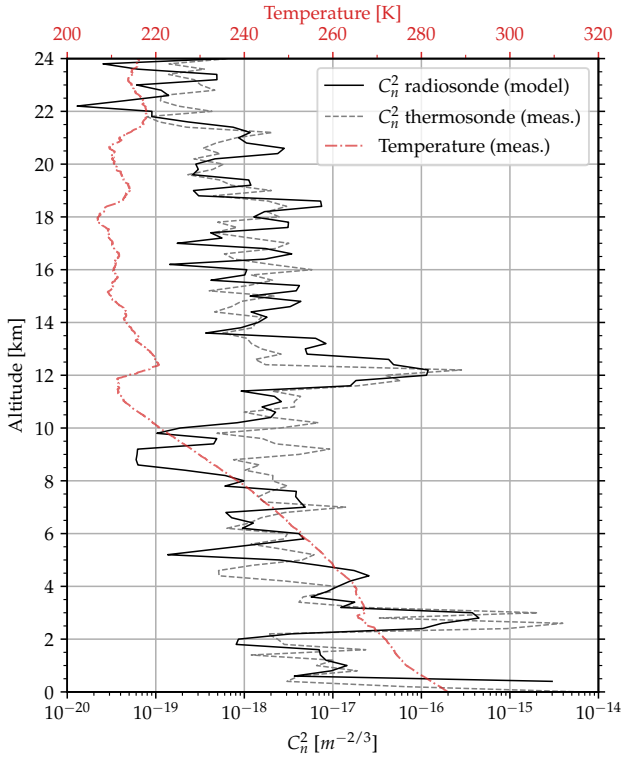


Fig. 10: C_n^2 profiles on March 31, 2006 at 00h48 UTC (T-REX019). The C_n^2 model used is the statistical definition model with $\Delta z = 200$ m.

profiles can be seen in Fig. 9, where the mentioned altitude is the altitude above the ground.

In the center and the right parts of this figure, two metrics have been added in order to quantify the performance of both C_n^2 models: the absolute bias and the root-mean-square error (RMSE). They are applied to the $\log_{10}(C_n^2)$, and their definitions are inspired from [28]:

$$\text{Absolute bias} = \sum_{i=1}^N \frac{|Y_i - X_i|}{N}, \quad (20)$$

$$\text{RMSE} = \sqrt{\sum_{i=1}^N \frac{(Y_i - X_i)^2}{N}}, \quad (21)$$

where N is the number of measurements ($N = 13$), X_i represents the i -th measurement of $\log_{10}(C_n^2)$ and Y_i is the logarithm in base 10 of the i -th modeled C_n^2 profile (either using the Tatarskii model of the statistical definition model). These metrics are function of the altitude z . Values obtained for both models are very similar, showing that the statistical definition C_n^2 model delivers C_n^2 estimates similar to the ones of Tatarskii-based models. Averaging over all altitudes, the absolute bias (resp. RMSE) for the Tatarskii model is 0.674 (resp. 0.842), whereas it is 0.683 (resp. 0.852) for the statistical definition model. Hence, according to these metrics, models have similar capabilities.

Furthermore, in Fig. 9, both modeled and measured C_n^2 profiles show the influence of the tropopause layer (close to 12 km of altitude) where they agree quite well. The decrease of C_n^2 in the troposphere is also identified. However, measurements show the presence of a turbulent layer close to the ground (2-3 km of altitude) that is not well depicted in the C_n^2 models. This effect comes from days when the magnitude

of the turbulent layer is underestimated. Indeed, as an example, the C_n^2 profile recorded on March 31, 2006 is given in Fig. 10. Isolated optical turbulent layers corresponding to temperature inversions can clearly be identified, in the thermosonde measurements as well as in the radiosonde model. This is similar to what has been observed in Fig. 8 for Hilo, HI, and in [37].

IV. DISCUSSION AND GENERALIZATION

This C_n^2 model, inspired by the statistical definition of C_n^2 in the inertial range, does not claim to be an accurate description of the physics of optical turbulence. Indeed, as previously introduced in Section II-C, the hypothesis of the inertial range, necessary for (13) to hold, may not be fulfilled given the available resolution of radiosonde measurements. Moreover, the model involves a fitted parameter that does not have a physical justification: the scaling factor.

Nevertheless, this model offers a simplified description of C_n^2 , easy to apply for practical scenarios. Despite its simplicity, it has also been shown in Section III-D that the accuracy of the model is comparable to other literature-based models, as long as it is calibrated accordingly.

Generalization of this approach to rely on physical scaling laws in the buoyancy range, i.e. the range made of scales larger than the outer scale L_0 , can be considered, and is of particular interest to obtain a model that may be free of fitting parameters. In the buoyancy range, different scaling laws of the temperature structure function have been proposed [38]–[40]. The hypotheses behind those different scaling laws are presented in [41], leading to temperature structure functions proportional to $\rho^{2/5}$ or ρ^2 in the buoyancy range.

V. CONCLUSION

A simple approach to estimate the optical C_n^2 profile based on its statistical definition has been presented, and compared with a Tatarskii-based model. This simple approach is made possible thanks to the use of high-density radiosonde profiles, and relies on the optical refractive index expression, involving only the pressure and the temperature profiles. From the refractive index vertical profile, refractive index fluctuations are extracted and C_n^2 is derived.

The use of recent high-density radiosonde profile at Trappes (France) and Hilo, HI (USA) showed the capability of the approach to obtain average C_n^2 profiles having similarities with well-known empirical profiles. This enabled to obtain site-dependent profiles using only classical radiosonde measurements, enabling further studies of geographical and seasonal variations of mean C_n^2 profiles. Furthermore, comparisons with thermosonde measurements showed good agreement and highlighted the possible identification of optical turbulent layers related to temperature inversions.

The main limitations of the approach are related to the input meteorological data used. Indeed, the scale of the turbulent structures that can be modeled is directly related to the available radiosonde vertical resolution. Moreover, radiosonde data are only available at some places in the world and at particular instants. A possible solution to this limitation is the

use of meteorological quantities coming directly from NWP simulations as inputs of the C_n^2 model.

DATA AVAILABILITY STATEMENT

Radiosonde data used in this research are publicly available in the University of Wyoming (UWYO) Atmospheric Science Radiosonde Archive. They can be accessed at <http://weather.uwyo.edu/upperair/bufr/aob.shtml>. Thermosonde measurements come from the T-REX campaign [34] and are accessible using <https://doi.org/10.26023/6HCG-E9WC-H0E>.

ACKNOWLEDGMENT

The University of Wyoming is thanked for the access to high-density radiosonde profiles through its website. AFRL and NCAR are thanked for the access to thermosonde data of the T-REX campaign. Data provided by NCAR/EOL under the sponsorship of the National Science Foundation, <https://data.eol.ucar.edu/>.

APPENDIX

For simplicity, a sketch of the proof is given in 1D. Assuming that the refractive index fluctuations $n_1(r)$ are sampled in the vertical direction, the equivalent sampled field $n_{1s}(r)$ is

$$\begin{aligned} n_{1s}(r) &= n_1(r) \sum_{k=-\infty}^{\infty} \delta(r - k\Delta z - z_0) \quad (22) \\ &= \sum_{k=-\infty}^{\infty} \underbrace{n_1(k\Delta z + z_0)}_{n_1[k]} \delta(r - k\Delta z - z_0), \quad (23) \end{aligned}$$

where $\delta(r)$ is the Dirac delta function, Δz is the sampling distance and z_0 is the initial position where sampling is started ($z_0 \in [0, \Delta z]$). This initial position is assumed to be random in order to make the sampled refractive index field homogeneous [42]. The discrete field is denoted $n_1[k]$.

With these homogeneity and one-dimensional fluctuation hypotheses, the structure function in the inertial range is given by [3]

$$D_n(\rho) = \langle (n_1(r + \rho) - n_1(r))^2 \rangle \quad (24)$$

$$= 2(B_n(0) - B_n(\rho)) = C_n^2 \rho^{2/3}, \quad (25)$$

where $B_n(\rho)$ is the covariance function which definition is

$$B_n(\rho) = \langle n_1(r + \rho) n_1(r) \rangle. \quad (26)$$

The covariance function of the sampled field is given by (27). Assuming that z_0 is known and independent of $n_1(r)$, the expectation can first be computed on n_1 and (28) is obtained, with $B_n[k - k']$ the discrete covariance function.

Then, the expectation on z_0 is taken, assuming z_0 is uniformly distributed between 0 and Δz such that its probability density function $T_{Z_0}(z_0)$ is

$$T_{Z_0}(z_0) = \begin{cases} \frac{1}{\Delta z} & \text{if } 0 \leq z_0 < \Delta z, \\ 0 & \text{otherwise.} \end{cases} \quad (30)$$

$$B_{n_s}(\rho) = \left\langle \left(\sum_{k=-\infty}^{\infty} n_1[k] \delta(r + \rho - k\Delta z - z_0) \right) \left(\sum_{k'=-\infty}^{\infty} n_1[k'] \delta(r - k'\Delta z - z_0) \right) \right\rangle, \quad (27)$$

$$B_{n_s}(\rho|z_0) = \sum_{k=-\infty}^{\infty} \sum_{k'=-\infty}^{\infty} \underbrace{\langle n_1[k] n_1[k'] \rangle}_{B_n[k-k']} \delta(r + \rho - k\Delta z - z_0) \delta(r - k'\Delta z - z_0). \quad (28)$$

$$\begin{aligned} B_{n_s}(\rho) &= \sum_{k=-\infty}^{\infty} \sum_{k'=-\infty}^{\infty} B_n[k-k'] \int_0^{\Delta z} \frac{1}{\Delta z} \delta(r + \rho - k\Delta z - z_0) \delta(r - k'\Delta z - z_0) dz_0 \\ &= \sum_{k=-\infty}^{\infty} \sum_{k'=-\infty}^{\infty} \frac{B_n[k-k']}{\Delta z} \int_{k'\Delta z - r}^{(k'+1)\Delta z - r} \delta(\rho - (k-k')\Delta z - s) \delta(s) ds \\ &= \sum_{k=-\infty}^{\infty} \frac{B_n[k-k^*]}{\Delta z} \delta(\rho - (k-k^*)\Delta z) \\ &= \sum_{i=-\infty}^{\infty} \frac{B_n[i]}{\Delta z} \delta(\rho - i\Delta z), \end{aligned} \quad (29)$$

This leads to the integration presented in (29), according to the definition of the expectation, and where the change of variable $s = k'\Delta z + z_0 - r$ has been used, as well as the fact that there exists only one value of k' (denoted k^*) such that $s = 0$ is in the integration domain and $\int_{k^*\Delta z - r}^{(k^*+1)\Delta z - r} \delta(s) ds = 1$. Finally, the change of variable $i = k - k^*$ is used.

In terms of structure function, (25) becomes

$$\begin{aligned} D_{n_s}(\rho) &= 2 \left(\sum_{i=-\infty}^{\infty} \frac{B_n[i]}{\Delta z} \delta(i\Delta z) - \sum_{i'=-\infty}^{\infty} \frac{B_n[i']}{\Delta z} \delta(\rho - i'\Delta z) \right) \\ &= C_n^2 \rho^{2/3}. \end{aligned} \quad (31)$$

Since $D_{n_s}(\rho)$ is only known for distances ρ multiple of the sampling distance, i.e. $\rho = m\Delta z$ with $m \in \mathbb{Z}$:

$$\begin{aligned} D_{n_s}(m\Delta z) &= 2 \left(\sum_{i=-\infty}^{\infty} \frac{B_n[i]}{\Delta z} \delta(i\Delta z) - \sum_{i'=-\infty}^{\infty} \frac{B_n[i']}{\Delta z} \delta((m-i')\Delta z) \right) \\ &= 2 \left(\frac{B_n[0]}{\Delta z} - \frac{B_n[m]}{\Delta z} \right) = C_n^2 (m\Delta z)^{2/3}, \end{aligned} \quad (32)$$

using the properties of the delta functions.

In practice, the structure function is computed in the discrete domain, i.e.

$$\begin{aligned} D_n[m] &= \langle (n_1[k+m] - n_1[k])^2 \rangle \\ &= \langle n_1^2[k+m] \rangle - 2 \langle n_1[k+m] n_1[k] \rangle + \langle n_1^2[k] \rangle \\ &= 2 (B_n[0] - B_n[m]). \end{aligned} \quad (33)$$

Using this last result and (32), our estimation of C_n^2 based on the discrete structure function is therefore

$$C_n^2 = \frac{1}{\Delta z} \frac{D_n[m]}{(m\Delta z)^{2/3}}. \quad (34)$$

This corresponds to (14) where the ergodicity hypothesis is used to compute the structure function $D_n[m]$ using a spatial average on 3 points.

REFERENCES

- [1] F. Roddier, "V the effects of atmospheric turbulence in optical astronomy," in *Progress in optics*, vol. 19, pp. 281–376, Elsevier, 1981.
- [2] G. Orban de Xivry, O. Absil, M. Lismont, V. Moreau, F. Languy, and D. Vanhoenacker-Janvier, "Preliminary design of salto: the belgian adaptive optics demonstrator," in *Adaptive Optics Systems VI*, vol. 10703, p. 1070338, International Society for Optics and Photonics, 2018.
- [3] V. I. Tatarskii, "The effects of the turbulent atmosphere on wave propagation," *Jerusalem: Israel Program for Scientific Translations*, 1971, 1971.
- [4] A. Ishimaru, *Wave propagation and scattering in random media*, vol. 2. Academic press New York, 1978.
- [5] L. C. Andrews and R. L. Phillips, *Laser Beam Propagation through Random Media, Second Edition*. SPIE Press, 2005.
- [6] A. Tokovinin, "From differential image motion to seeing," *Publications of the Astronomical Society of the Pacific*, vol. 114, no. 800, p. 1156, 2002.
- [7] E. M. Dewan, *A Model for C2n (optical turbulence) profiles using radiosonde data*. No. 1121, Directorate of Geophysics, Air Force Materiel Command, 1993.
- [8] R. E. Hufnagel, *The Infrared Handbook - Propagation through atmospheric turbulence (Chapter 6)*. SPIE Press, 1985.
- [9] S. Basu, J. Osborn, P. He, and A. DeMarco, "Mesoscale modelling of optical turbulence in the atmosphere: the need for ultrahigh vertical resolution," *Monthly Notices of the Royal Astronomical Society*, vol. 497, no. 2, pp. 2302–2308, 2020.
- [10] E. Masciadri, F. Lascaux, A. Turchi, and L. Fini, "Optical turbulence forecast: ready for an operational application," *Monthly Notices of the Royal Astronomical Society*, vol. 466, no. 1, pp. 520–539, 2017.
- [11] Y. Karasawa, M. Yamada, and J. E. Allnutt, "A new prediction method for tropospheric scintillation on earth-space paths," *IEEE transactions on antennas and propagation*, vol. 36, no. 11, pp. 1608–1614, 1988.
- [12] V. Fabbro, N. Jeannin, K. Djafri, J. Lemorton, and D. Vanhoenacker-Janvier, "Scintillation modelling in troposphere using multiple phase screen," *Space communications*, vol. 22, no. 2-4, pp. 51–57, 2013.
- [13] E. Martini, A. Freni, F. Cuccoli, and L. Facheris, "Derivation of clear-air turbulence parameters from high-resolution radiosonde data," *Journal of Atmospheric and Oceanic Technology*, vol. 34, no. 2, pp. 277–293, 2017.
- [14] H. Vasseur, "Prediction of tropospheric scintillation on satellite links from radiosonde data," *IEEE Transactions on Antennas and Propagation*, vol. 47, no. 2, pp. 293–301, 1999.
- [15] D. Vanhoenacker-Janvier, L. Quibus, M. Rytir, and T. Tjelta, "Measurement and modelling of tropospheric scintillation in ka/q band," in *2017 11th European Conference on Antennas and Propagation (EUCAP)*, pp. 1486–1490, IEEE, 2017.

- [16] H. Trinquet and J. Vernin, "A statistical model to forecast the profile of the index structure constant c_n^2 ," *Environmental Fluid Mechanics*, vol. 7, no. 5, pp. 397–407, 2007.
- [17] A. Abahamid, A. Jabiri, J. Vernin, Z. Benkhalidoun, M. Azouit, and A. Agabi, "Optical turbulence modeling in the boundary layer and free atmosphere using instrumented meteorological balloons," *Astronomy & Astrophysics*, vol. 416, no. 3, pp. 1193–1200, 2004.
- [18] L. Montoya, J. De La Rosa, J. Castro-Almazán, I. Montilla, and M. Collados, "Modeling day time turbulence profiles: application to teide observatory," *Adaptive Optics for Extremely Large Telescopes (AO4ELT5)*, 2017.
- [19] C. Bi, X. Qian, Q. Liu, W. Zhu, X. Li, T. Luo, X. Wu, and C. Qing, "Estimating and measurement of atmospheric optical turbulence according to balloon-borne radiosonde for three sites in china," *JOSA A*, vol. 37, no. 11, pp. 1785–1794, 2020.
- [20] R.-R. Belu and G. Jumper, "Comparison of the refractive index structure constant prediction using radiosonde data to in-situ thermosonde measurements," in *2012 9th International Conference on Communications (COMM)*, pp. 147–150, IEEE, 2012.
- [21] C. Qing, X. Wu, X. Li, T. Luo, C. Su, and W. Zhu, "Mesoscale optical turbulence simulations above tibetan plateau: first attempt," *Optics express*, vol. 28, no. 4, pp. 4571–4586, 2020.
- [22] N. M. Gavrilov, H. Luce, M. Crochet, F. Dalaudier, and S. Fukao, "Turbulence parameter estimations from high-resolution balloon temperature measurements of the mutsi-2000 campaign," in *Annales Geophysicae*, vol. 23, pp. 2401–2413, Copernicus GmbH, 2005.
- [23] S. Basu, "A simple approach for estimating the refractive index structure parameter (Cn2) profile in the atmosphere," *Optics letters*, vol. 40, no. 17, pp. 4130–4133, 2015.
- [24] S. Wu, C. Su, X. Wu, T. Luo, and X. Li, "A Simple Method to Estimate the Refractive Index Structure Parameter (C_n^2) in the Atmosphere," *Publications of the Astronomical Society of the Pacific*, vol. 132, no. 1014, p. 084501, 2020.
- [25] R. R. Beland and J. H. Brown, "A deterministic temperature model for stratospheric optical turbulence," *Physica Scripta*, vol. 37, no. 3, p. 419, 1988.
- [26] T. Cherubini and S. Businger, "Another look at the refractive index structure function," *Journal of applied meteorology and climatology*, vol. 52, no. 2, pp. 498–506, 2013.
- [27] F. H. Ruggiero and D. A. DeBenedictis, "Forecasting optical turbulence from mesoscale numerical weather prediction models," in *DoD High Performance Modernization Program Users Group Conference*, pp. 10–14, 2002.
- [28] M. Xu, S. Shao, N. Weng, and Q. Liu, "Analysis of the optical turbulence model using meteorological data," *Remote Sensing*, vol. 14, no. 13, p. 3085, 2022.
- [29] C. Coulman, J. Vernin, Y. Coqueugniot, and J. Caccia, "Outer scale of turbulence appropriate to modeling refractive-index structure profiles," *Applied Optics*, vol. 27, no. 1, pp. 155–160, 1988.
- [30] V. P. Lukin, "Outer scale of atmospheric turbulence," in *Optics in Atmospheric Propagation and Adaptive Systems VIII*, vol. 5981, p. 598101, International Society for Optics and Photonics, 2005.
- [31] J. W. Hardy, *Adaptive optics for astronomical telescopes*, vol. 16. Oxford University Press, 1998.
- [32] S. Laroche and R. Sarrazin, "Impact of radiosonde balloon drift on numerical weather prediction and verification," *Weather and forecasting*, vol. 28, no. 3, pp. 772–782, 2013.
- [33] C. Coulman, J.-C. Andre, P. Lacarrere, and P. Gillingham, "The observation, calculation, and possible forecasting of astronomical seeing," *Publications of the Astronomical Society of the Pacific*, vol. 98, no. 601, p. 376, 1986.
- [34] Jumper, G., "T-REX: AFRL Radiosonde and Thermosonde Data." 2007. Version 1.0. UCAR/NCAR - Earth Observing Laboratory. <https://doi.org/10.26023/6HCG-E9WC-H0E>. Accessed 25 June 2021.
- [35] Jumper, G., "Thermosonde and radiosonde data from the T-REX campaign," 2006. Documentation from <https://data.eol.ucar.edu/dataset/92.048>.
- [36] Beland, R. R., "Propagation through atmospheric optical turbulence," in *The Infrared & Electro-optical Systems Handbook* (F. G. Smith, ed.), vol. 2, ch. 2, pp. 157–224, SPIE Optical Engineering Press, 1993.
- [37] A. Mahalov and M. Moustauoui, "Characterization of atmospheric optical turbulence for laser propagation," *Laser & Photonics Reviews*, vol. 4, no. 1, pp. 144–159, 2010.
- [38] R. Bolgiano Jr, "Structure of turbulence in stratified media," *Journal of Geophysical Research*, vol. 67, no. 8, pp. 3015–3023, 1962.
- [39] C. Cot and J. Barat, "Spectral analysis of high resolution temperature profiles in the stratosphere," *Geophysical Research Letters*, vol. 16, no. 10, pp. 1165–1168, 1989.
- [40] G. Nastrom, T. Van Zandt, and J. Warnock, "Vertical wavenumber spectra of wind and temperature from high-resolution balloon soundings over illinois," *Journal of Geophysical Research: Atmospheres*, vol. 102, no. D6, pp. 6685–6701, 1997.
- [41] S. Basu and A. A. Holtslag, "Revisiting and revising tatarskii's formulation for the temperature structure parameter (c_T^2) in atmospheric flows," *Environmental Fluid Mechanics*, vol. 22, no. 5, pp. 1107–1119, 2022.
- [42] A. Leon-Garcia, *Probability and random processes for electrical engineering*. Pearson Education India, 1994.